Fracture mechanisms and microstructure in a medium Mn quenching and partitioning steel exhibiting macrosegregation

Hidalgo Garcia, Javier; Alonso de Celada Casero, Carola; Santofimia Navarro, Maria

DOI
10.1016/j.msea.2019.03.055

Publication date
2019

Document Version
Final published version

Published in
Materials Science and Engineering A

Citation (APA)
Hidalgo Garcia, J., Alonso de Celada Casero, C., & Santofimia Navarro, M. (2019). Fracture mechanisms and microstructure in a medium Mn quenching and partitioning steel exhibiting macrosegregation. *Materials Science and Engineering A*, *754*, 766-777. https://doi.org/10.1016/j.msea.2019.03.055

Materials Science & Engineering A 754 (2019) 766–777

Contents lists available at ScienceDirect

Materials Science & Engineering A

journal homepage: www.elsevier.com/locate/msea

Fracture mechanisms and microstructure in a medium Mn quenching and partitioning steel exhibiting macrosegregation

J. Hidalgo*, C. Celada-Casero, M.J. Santofimia

Department of Materials Science and Engineering, Delft University of Technology, Mekelweg 2, 2628 CD, Delft, the Netherlands

ARTICLE INFO

Keywords:
Quenching and partitioning
Medium manganese steels
Microstructure
Fracture mechanisms

ABSTRACT

A medium-Mn steel, exhibiting manganese macrosegregation, was investigated. In order to study how the microstructure development influences the fracture mechanisms, the steel was quenching and partitioning processed using two different partitioning temperatures. At 400 °C partitioning temperature, the microstructure exhibits intergranular fracture at low plastic strain, following Mn-rich regions in which fresh martensite predominates. Elongated thin precipitates at prior austenite grain boundaries facilitate the initiation and progress of cracks at these locations. After partitioning at 500 °C, the redistribution of carbon triggers the formation of pearlite, the precipitation of carbides in the carbon-enriched austenite and the formation of spheroidal carbides at prior austenite grain boundaries. All these microstructural features result in an interlath fracture with more ductile character than after partitioning at 400 °C. In both cases, manganese macrosegregation triggers brittle fracture mechanisms by creating large hardness gradients.

1. Introduction

Driven by weight-saving and safety demands from the automotive industry, the last decades were marked by the introduction of multiphase advanced high-strength steels (AHSS) [1]. Quenching and Partitioning (Q&P) steels are framed within this category. After full or intercritical austenitisation, the Q&P processing involves quenching to a temperature (T_Q) within the range of start-finish martensite temperature (M_S-M_F), which ensures the controlled formation of primary martensite (M1), and isothermal holding at a partitioning temperature (T_P) equal or higher than T_Q, in which the untransformed austenite is stabilised by carbon enrichment coming from M1. Other parallel processes such as primary martensite tempering and decomposition of austenite into bainite compete for the available carbon at T_P [2,3]. Under these considerations, partitioning at 400 °C has shown to be adequate for carbon enrichment in austenite for most Q&P steel compositions [4,5]. If the austenite is not sufficiently enriched in carbon during the partitioning stage, it transforms into fresh martensite (M2) during the final quench of the Q&P process. The presence of fresh martensite in the microstructure is associated with a reduction of elongation and worsening of properties in Q&P steels [6,7].

The good properties of the Q&P microstructures result from the combination of martensite and retained austenite that provides high-strength, toughness and ductility. The selection of T_Q, T_P and partitioning time (t_P) influences the Q&P microstructure and, consequently, the mechanical properties of the steel [8,9]. In this sense, the retained austenite (RA) volume fraction and its mechanical stability are important microstructural parameters. In principle, a high RA fraction is desirable to obtain an elevated work-hardening at high strains. This leads to improved ductility, formability and impact energy absorption via the mechanical induced transformation of austenite [1,10,11].

Medium manganese steels are interesting systems to carry out Q&P processes. Other than their low hardenability and retardation of bainite formation, they have a great potential to utilize both carbon and manganese in the austenite stabilisation process under adequate partitioning conditions [12,13]. This requires an increase of typical partitioning temperatures to promote sufficient mobilisation of Mn. However, this temperature increase might trigger other microstructural processes. On the other hand, medium Mn martensitic steels tend to undergo strong embrittlement when they are tempered in the temperature range of 300–500 °C and times from few minutes to hours [14–22]. The main reason for embrittlement points to Mn segregation to prior austenite grain boundaries, which decreases their cohesion strength and causes intergranular fracture [18,20,21].

In addition, Mn-rich steels have high probability of Mn macrosegregation since Mn is rejected into dendritic spaces during solidification after casting [2,23,24]. Hot deformation can be applied to break the dendritic structure of the cast ingot, which results in the segregation

* Corresponding author.
E-mail addresses: J.HidalgoGarcia@tudelft.nl (J. Hidalgo), C.CeladaCasero@tudelft.nl (C. Celada-Casero), M.J.SantofimiaNavarro@tudelft.nl (M.J. Santofimia).

https://doi.org/10.1016/j.msea.2019.03.055
Received 29 January 2019; Accepted 11 March 2019
Available online 14 March 2019

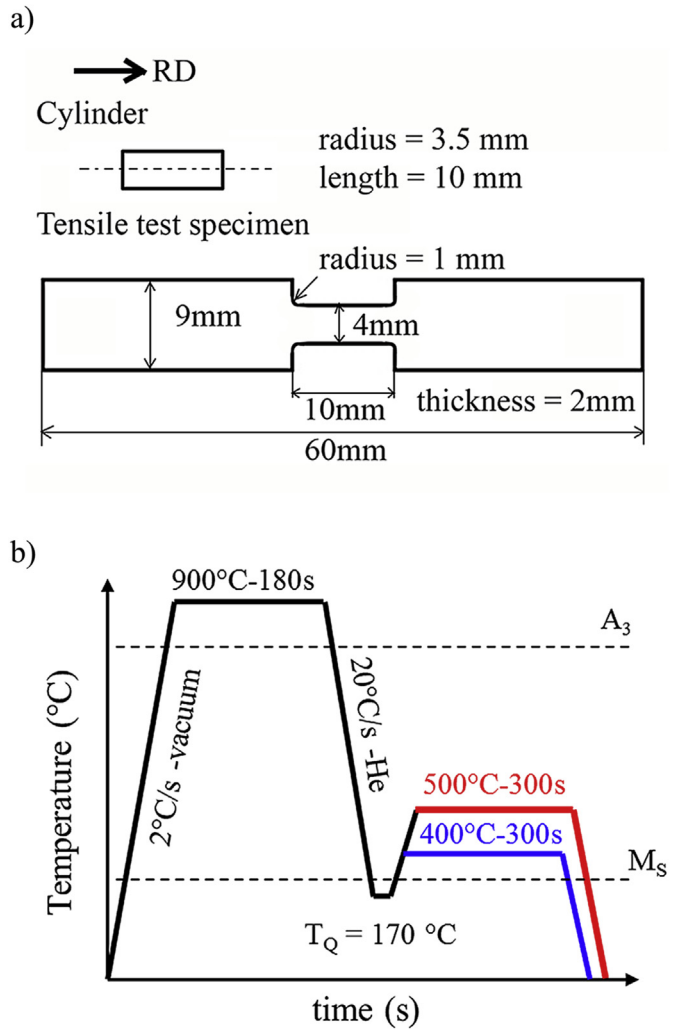

Fig. 1. (a) Dimensions of the cylindrical and tensile specimens. (b) Heat treatments applied to the steel.

aligned following the hot deformation direction [25,26]. Permanent elimination of Mn segregation requires long high-temperature homogenisation treatments due to the slow kinetics of Mn diffusion [25], which may result economically infeasible. Therefore, the impact of Mn segregation needs to be minimised by an adequate microstructure design.

This study addresses the effect of Mn segregation on the microstructural development of a medium-Mn steel during the Q&P processing route. The microstructural processes that take place during low and high partitioning temperatures are investigated based on experimental characterisation and local carbon redistribution simulations. Finally, fracture mechanisms are related with resulting microstructures.

2. Experimental methodology

A medium manganese steel with chemical composition of 0.3C–4.5Mn-1.5Si (wt. %) in the form of cast and forged billets was investigated. Cylindrical and tensile dilatometry samples, as shown in Fig. 1a, were machined from the billet. A Bähr DIL 805 A/D dilatometer was used to carry out different heat treatments in both cylindrical and tensile samples and to characterize the events occurring during the heat treatments. Two different quenching and partitioning treatments were carried out to develop different microstructures as shown in Fig. 1b. In all thermal cycles, the specimens were first fully austenitized at 900 °C for 3 min. Then, specimens were cooled down at 20 °C/s to a T_Q = 170 °C. Subsequently, the specimens were held at T_P = 400 °C or 500 °C for 300 s. The specimens are designated as QPT_P. Final cooling to room temperature was done at 20 °C/s.

Resulting microstructures were resolved by light optical and scanning electron microscopy (LOM and SEM). Specimens of each heat treatment were metallographically prepared with a final polishing step of 1 µm. The SEM study was made after etching with 2% Nital, using a JEOL JSM-6500F field emission gun scanning electron microscope (FEG-SEM) operating at 15 kV.

The final fraction of retained austenite was obtained from magnetization saturation measurements carried out at room temperature in a vibrating sample magnetometer (VSM) 7307 manufactured by Lake Shore and calibrated with a standard NIST nickel specimen. Cubic specimens with an edge dimension of 2.0 mm were machined from the centre of the dilatometry specimens. The procedure followed is derived from the methods described in Refs. [27–29]. The volume fraction of retained austenite is calculated as $f_{RA} = 1 - M_{sat}{}^{QP}/(x_{Fe}{\cdot}M_{sat}{}^{\alpha-Fe})$, where $M_{sat}{}^{QP}$ is the magnetization saturation of the Q&P specimen, x_{Fe} is the iron content of the steel and $M_{sat}{}^{\alpha-Fe}$ is the magnetization saturation of pure bcc iron, which yields 215 Am^2/kg at room temperature [30].

X-Ray diffraction (XRD) experiments were performed to estimate the carbon content in austenite. A Bruker D8 Advance Diffractometer equipped with a Vantec position sensitive detector was employed, using Co Kα1 radiation with a wavelength of λ = 1.78897 Å, an acceleration voltage of 45 kV and current of 35 mA, while the sample was spinning at 30 rpm. The measurements were performed in the Bragg's angle (2θ) range of 40°–130°, using a step size of 0.042° 2θ, with a counting time per step of 3 s. The carbon concentration within the retained austenite, $x_C{}^{RA}$, was determined from its lattice parameter a_γ, (in Å) as [31]:

$$a_\gamma = 3.556 + 0.0453x_C + 0.00095x_{Mn} + 0.0056x_{Al} \quad (1)$$

where x_i, in wt. %, represents the concentration of the alloying element *i*. The Nelson-Riley method [32] was used to determine the lattice parameter of austenite.

Vickers 0.01 Kg micro-hardness was measured with a Struers Durascan tester to characterize heterogeneities of hardness across the microstructure. Two tensile tests were performed per condition with an Instron testing frame and an extensometer with a 7.8 mm gauge length at an engineering strain rate of $6{\cdot}10^{-3}$ s^{-1}. The fraction of austenite remaining after tensile tests was determined with VSM in all the tested specimens.

Electron probe microanalysis (EPMA) was performed with a JEOL JXA 8900R microprobe using an electron beam with energy of 10 keV and beam current of 200 nA employing Wavelength Dispersive Spectrometry (WDS). The composition at each analysis location of the specimen was determined using the X-ray intensities of the constituent elements after background correction relative to the corresponding intensities of reference materials. The obtained intensity ratios were processed with a matrix correction program CITZAF [33].

3. Results

3.1. Phase mixture

The dilatometry curves of specimens QP400 and QP500 are shown in Fig. 2a as a function of temperature. The volume fractions of primary and secondary martensite phases were obtained by applying the lever rule and using the linear expansion behaviour of the fcc and bcc lattices in the dilatometry curves, as schematized in Fig. 2b. Table 1 shows the volume fraction and carbon content of retained austenite present in the final Q&P microstructures.

As can be seen in Fig. 2a, primary martensite (M1) starts forming at 235 ± 5 °C (labelled as $M1_S$). A volume fraction of M1 of 0.60 is formed during the first quench to 170 °C. Then, the material is heated up to the partitioning temperature. Fig. 2c displays the change in length with partitioning time at 400 °C and 500 °C partitioning temperatures.

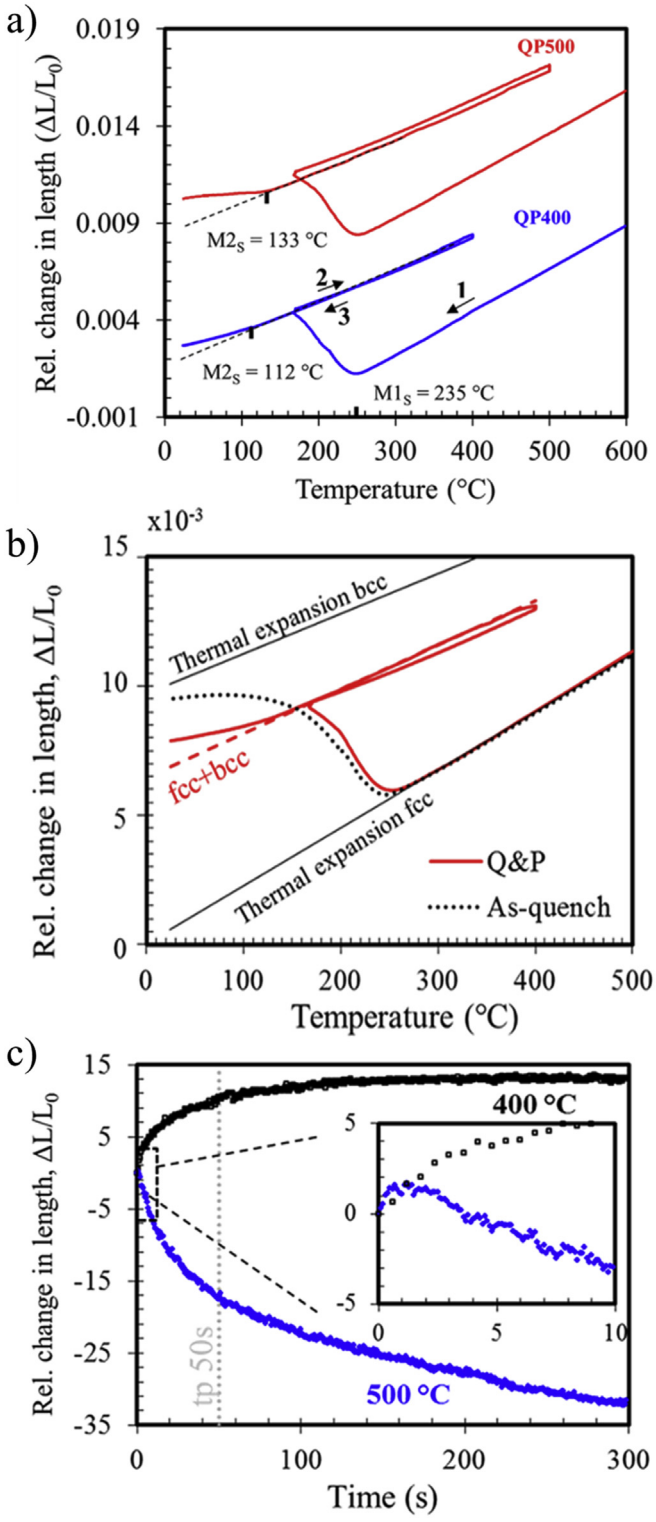

Fig. 2. (a) Dilatometry curves vs. temperature of the different Q&P heat treatments. $M1_S$ and $M2_S$ stand for the primary and fresh martensite start temperatures, respectively. (b) Comparative of as-quench and Q&P dilatometry curves with temperature in which thermal expansion lines of bcc and fcc phases are fitted to the experimental curves. (c) Dilatometry curves vs. time during partitioning stage.

A slight expansion is registered during partitioning at 400 °C, which is typical of carbon enrichment in austenite due to partitioning and suggests a negligible formation of bainite [34]. Instead, partitioning at 500 °C leads to an initial small expansion (zoomed-in in the inset) followed by a shrinkage. After the partitioning stage, the material is cooled to room temperature. Deviations from linearity during the final quench evidence the formation of fresh martensite, whose start temperature is labelled as $M2_S$. Table 1 shows that $M2_S$ is about 10 °C higher in QP500 than in QP400 specimen. This fact indicates a lower austenite stability after partitioning at 500 °C, which is also evidenced by the considerably higher fractions of M2 in comparison with QP400. A retained austenite fraction of 0.29 was measured in QP400, which doubles that of QP500. The carbon concentration in austenite is also higher in QP400 than in QP500. The volume fraction of carbides or other phases was balanced from the martensite and austenite fractions.

Table 1
Summary of volume fractions and carbon content of phases.

T_P °C	$M1_S$ °C	$M2_S$ °C	f_{M1}	f_{RA}	f_{M2}	$f_{balance}$ carbide/pearlite	x_C^{RA} wt.%
400	235 ± 5	112 ± 5	0.60	0.29	0.10	0.01	0.80
500	235 ± 5	133 ± 5	0.60	0.14	0.17	0.09	0.62

3.2. Microstructural characterisation

Light optical micrographs in Fig. 3a&b evidence a heterogeneous microstructure in QP400 and QP500 specimens, respectively. Crossing bands of a light etched constituent are entangled with dark etched

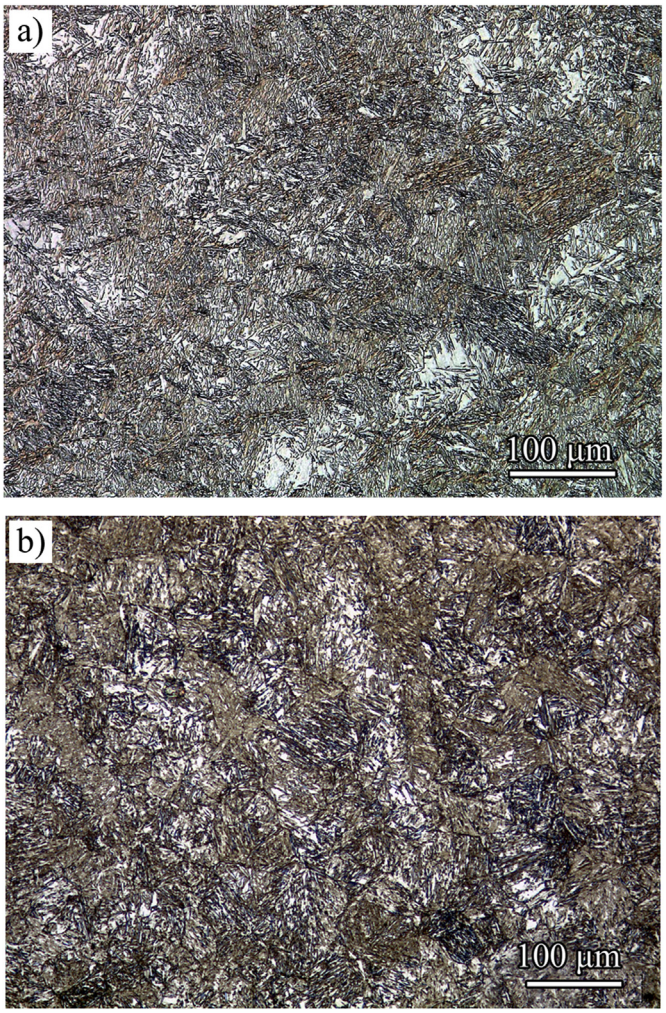

Fig. 3. LOM micrographs of over etched (a) QP400 and (b) QP500 to highlight the heterogeneous microstructure in bands.

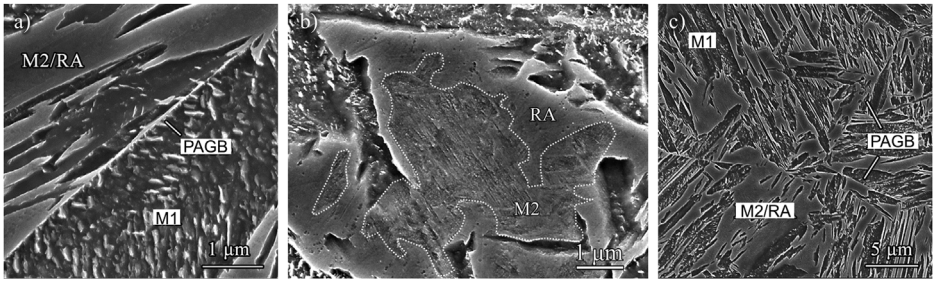

Fig. 4. SEM micrographs of QP400 (a) low (b) high magnification. Retained austenite (RA), primary and secondary martensite (M1, M2), are pointed.

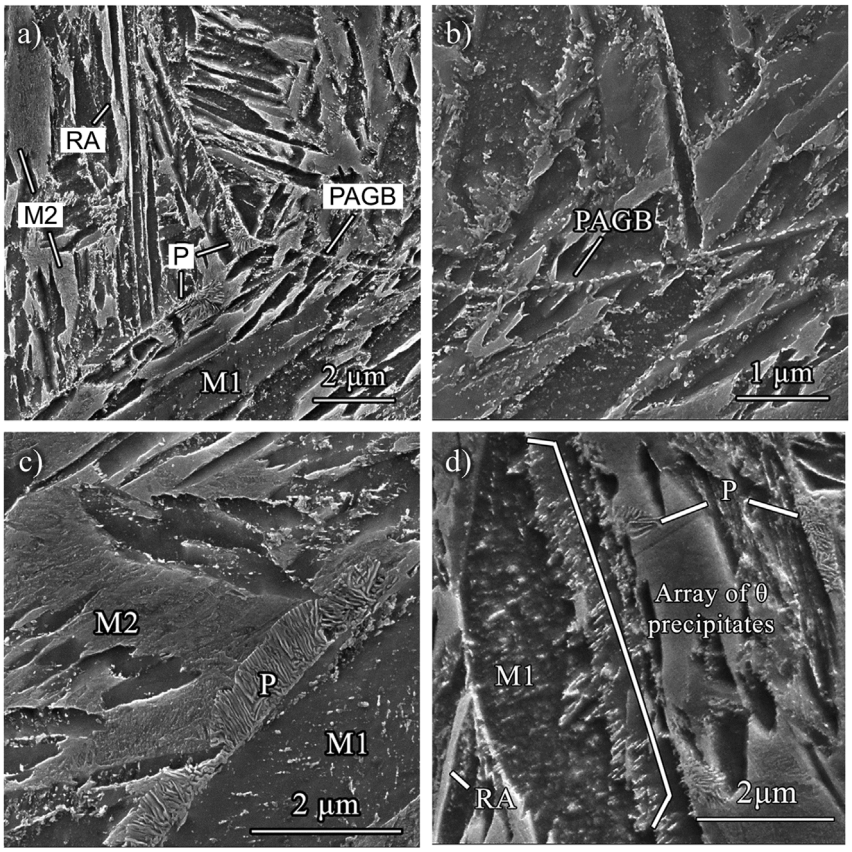

Fig. 5. SEM micrographs of QP500 (a) low (b), (c), and (d) high magnification. Retained austenite (RA), primary and secondary martensite (M1, M2), pearlite (P) and cementite precipitates (θ) are pointed.

regions. The pattern resembles a former dendritic structure developed during cast solidification. Fig. 4 and Fig. 5 show SEM micrographs of the Q&P microstructures obtained at partitioning temperatures of 400 °C and 500 °C, respectively. In Fig. 4, the primary martensite matrix is characterised by the presence of most likely transitional needle-type carbides parallel to specific habit planes within martensite blocks substructures. These kind of carbides were also observed in a condition directly quenched to room temperature after austenitisation, which suggests that they precipitate as consequence of the auto-tempering in martensite. As typical of Q&P microstructures, the RA is present in a film-like morphology in between laths of primary martensite, and in a blocky-like morphology next to prior austenite grain boundaries (PAGBs) or to packet and block boundaries of martensite [35]. Fresh martensite/retained austenite (M2/RA) islands in the micrometre scale are observed heterogeneously distributed in the microstructure. These M2/RA islands are less etched than the primary martensite phase due to their higher carbon content [36]. Increasing the etching time discloses the fresh martensite (outlined with a dotted line in Fig. 4b), which is surrounded by large grains of retained austenite in a ring-like configuration. The fresh martensite is characterised by a very thin lath structure. The ring-like configuration originates from an incomplete homogenisation of carbon across the austenite grain during the partitioning step, which is usual in large grains. Prior austenite grain boundaries are vaguely distinguishable, particularly when the boundary is shared by two M2/RA islands. Continuous film-like features of tens of nanometres in width are usually observed delimiting two adjacent M1 blocks sharing a PAGB, as pointed by arrows in Fig. 4c. This feature might be a carbide. It is well known that prior austenite grain boundaries are preferential nucleation sites of carbides during tempering of martensite [15,37]. These carbides form as very thin films during the first stages of tempering and are typically difficult to detect [38]. When a PAGB is shared by two M1 blocks, the carbon segregates preferentially to the boundary from both sides promoting the formation of the carbide. Instead, when the PAGB is shared by martensite and austenite, part of the carbon diffuses into the austenite. This makes improbable the formation of the continuous carbide at these locations.

Fig. 5 shows SEM micrographs of the Q&P microstructures partitioned at 500 °C. Several differences from conventional Q&P

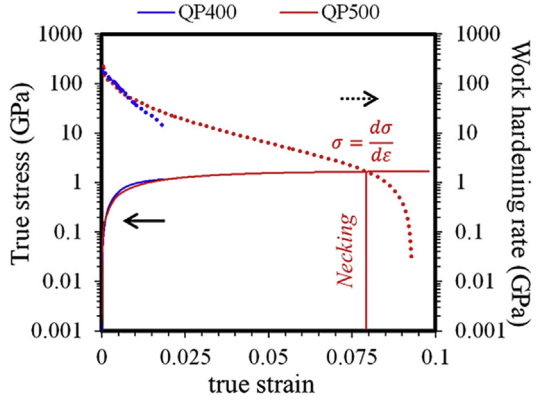

Fig. 6. True stress (solid lines) and work hardening rate (dotted lines) as a function of true strain of QP400 and QP500.

microstructures are observed. On the one hand, the clear definition of the PAGBs is eye-catching. Higher magnifications reveal that spherical carbides decorate the PAGBs (Fig. 5b), which allows to estimate the prior austenite grain size in about 30 µm. The higher partitioning temperature of 500 °C promotes the formation of coarse and spherical carbides at PAGBs instead of the continuous film carbide that forms at 400 °C. In addition to the spherical carbides, pearlite colonies are observed next to the PAGBs, as observed in Fig. 5c. The same figure shows that carbides in M1 are coarser and more globular than those observed in QP400. The coarsening and spheroidization of the carbides in martensite is also commonly observed at advanced stages of tempering in steels [38]. Additionally, Fig. 5d shows the presence of arrays of elongated parallel carbides at some locations next to PAGBs, at interfaces between primary martensite and RA blocks or in between laths of M1 replacing what it seems to be austenite films. As Fig. 5c shows, M2/RA blocks in QP500 are mainly composed of M2. The blocky-type of RA is seldom distinguishable.

3.3. Mechanical properties

Fig. 6a shows the evolution of the true stress (solid lines) and work hardening rate (dotted lines) with the true strain of QP400 and QP500 conditions. Relevant tensile properties are shown in Table 2. Both specimens exhibit similar behaviour until 0.01 deformation, after which the QP500 specimen shows a higher work-hardening rate. It is worth mentioning that QP400 breaks well before the necking condition, $\sigma = d\sigma/d\varepsilon$. With a lower $\sigma_{y0.2}$, the QP500 condition exhibits much higher ultimate tensile strength (UTS), total elongation (TE) and work hardening than the QP400 specimen. The uniform elongation (UE) almost coincides with the TE. It is striking that the QP400 specimen present a higher RA fraction with a higher carbon content than QP500 and yet, its mechanical performance is worse. These results contradict the general understanding on Q&P steels, where high fractions of RA are sought to improve the ductility [6].

3.4. Fracture surfaces

Fig. 7a–b shows SEM images of the fracture surface of the QP400 microstructure after tensile testing. It can be observed that the fracture

Table 2
Mechanical properties and fraction of retained austenite after fracture.

	$\sigma_{y0.2}$ *MPa*	UTS *MPa*	TE	UTS*TE MPa	f_{RA}^{F}
QP400	800	1100	0.02	22	0.19 ± 0.01
QP500	610	1530	0.10	153	0.02 ± 0.01

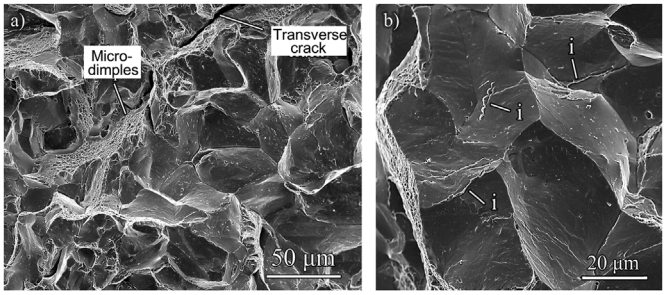

Fig. 7. Fractography of tensile tested QP400 specimen.(a) General overview. (b) Detail of intergranular fracture: i) Elongated/plate-like precipitates.

mainly progresses along the prior austenite grain boundaries. This mechanism is known as intergranular fracture [39] and is usually caused by impurities segregation to the grain boundaries or by a processing problem like quench cracking [40]. The occurrence of intergranular fracture indicates that grain boundaries are so weakened that prior austenite grain detachment occurs before any plastic deformation can take place. The intergranular fracture leaves smooth facets revealing the morphology and size of the prior austenite grains. In addition, secondary cracks perpendicular to the fracture surface also indicate brittleness of the grain boundaries. As can be observed from Fig. 7a, regions of intergranular fracture appear connected to one another by regions of ductile fracture, where micro-dimples are present. Dimples are the result of plastic deformation due to the transgranular progress of the crack during failure and evidence localized ductility. These observations indicate competition between intergranular and transgranular fracture in the microstructure partitioned at 400 °C. Features resembling plate-like and elongated precipitates are commonly observed standing out the fracture surfaces or in the intersection between adjacent prior austenite grains. This features are indicated by arrows in Fig. 7b.

Fig. 8 shows the fractography of the specimen partitioned at 500 °C. Mixed characteristics of brittle and ductile fracture are observed. In both cases the crack propagates transgranularly. During dominant brittle fracture (cleavage), the crack propagates through crystallographic planes, which produces flat and smooth surfaces (cleavage planes) decorated with river-like features. A fine-faceted crack structure (labelled in Fig. 8b–c) is observed in regions where cleavage occurs, which reveals a cleavage detaching mechanisms at predominantly martensite block boundaries. Several deep cracks are also visible. On the other hand, fracture features that are revealed lighter under the SEM indicate significant ductile failure, where micro-dimples are observed. Large dimples are also sporadically observed.

4. Discussion

4.1. Microstructure evolution during partitioning

Figs. 4 and 5 have shown that different microstructural evolution processes take place at the partitioning temperatures of 400 and 500 °C. It is well-known that partitioning at 400 °C promotes the diffusion of carbon from M1 to the adjacent austenite [41]. However, carbon partitioning temperatures as high as 500 °C promote a different development of the microstructure that, in the steel under investigation, leads to pearlite formation and precipitation within austenite films. To understand the microstructural mechanisms that activate at 500 °C, simulations of the carbon redistribution between martensite and austenite were carried out using DICTRA software [42]. The simulation system is defined as a martensite lath of 0.2 µm in width and a film of austenite of 100 nm in thickness [43–45], which are in contact through a planar martensite/austenite interface. Simulations were performed at 400 and 500 °C and for partitioning times up to 300 s). The results are

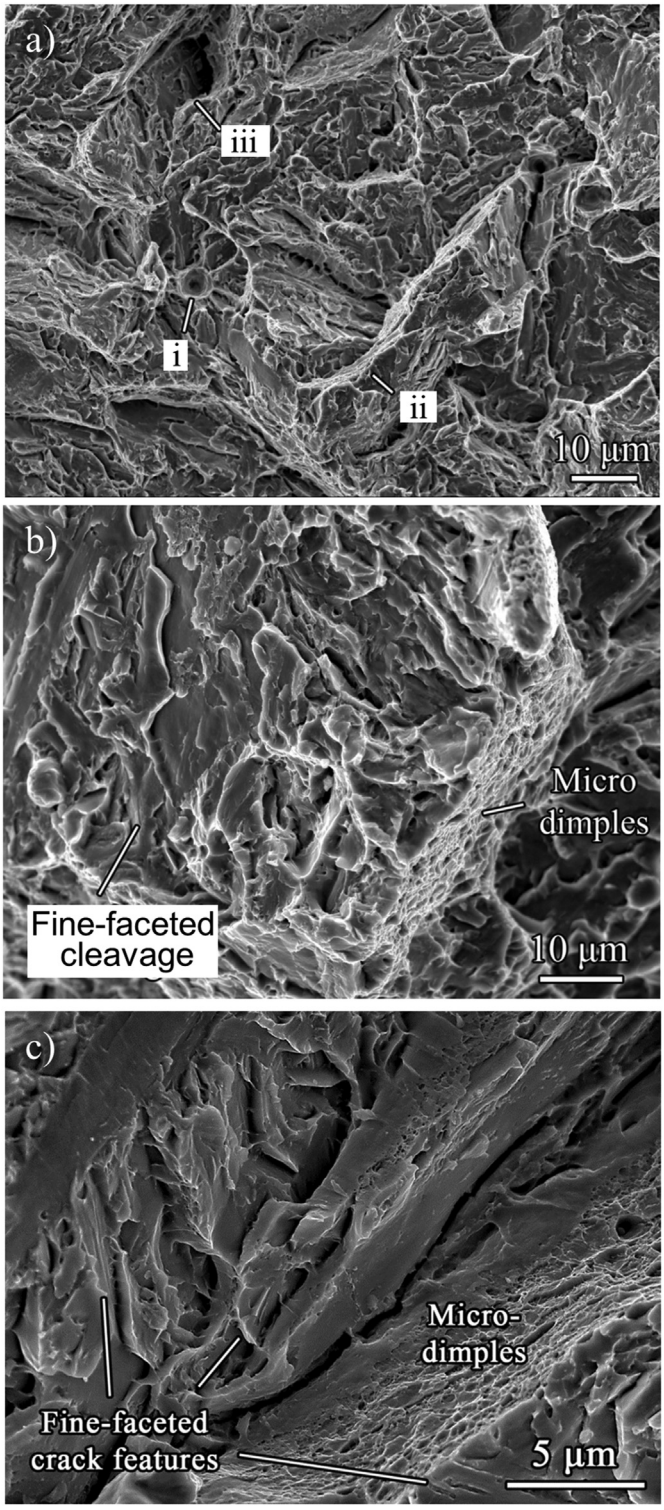

Fig. 8. Fractography of tensile tested QP500 specimen. (a) General overview: i) dimple, ii) ductile character region, iii) deep crack. (b) Detail of transgranular faceted fracture. (c) Detail of a deep crack.

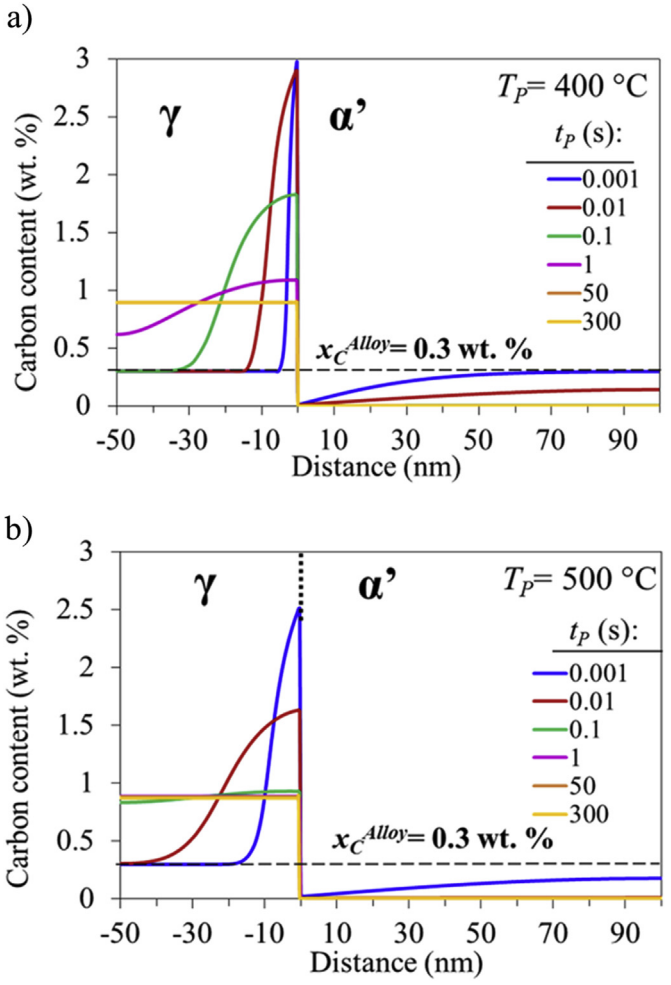

Fig. 9. Carbon profiles at different t_P for both T_P calculated by DICTRA. The γ/α′ interface is located at distance zero. Thus, negative and positive values of distance represent half lath width of austenite and martensite, respectively. x_C^{Alloy} and $x_C^{\gamma+}$ stand for the carbon content before partitioning and the critical carbon content required for the austenite to decompose into cementite and carbon-depleted austenite, respectively.

shown in Fig. 9 and discussed based on dilatometry (Fig. 2c) and on the carbon profiles for each partitioning temperature:

Partitioning at 400 °C: Dilatometry (Fig. 2c) shows a progressive expansion during the first 50 s that progresses to a saturation value before 300 s. Bainite or isothermal martensite are not likely to form upon the studied partitioning conditions due to the austenite stabilizing effect of manganese. Hence, an expansion of such magnitude is attributed to carbon partitioning and γ/α' interfaces migration [34]. DICTRA simulations predict full carbon partitioning and homogenisation in the austenite after 50 s (Fig. 9a). The carbon content in austenite is predicted to be around 0.80 wt %, which matches the experimental XRD results. However, the continuous expansion detected by dilatometry between 50 s and 300 s of partitioning time indicates that the redistribution of carbon is not complete after 50 s. This was experimentally verified by creating a specimen in which the partitioning treatment was interrupted after 50 s. Under these conditions, a lower carbon content was measured in the retained austenite (0.72 ± 0.02 wt %) and a higher M2 fraction (0.10 ± 0.01) was detected in the microstructure compared to that obtained after 300 s. These results indicate that, although the carbon partitioning process might be completed after 50 s in austenite films up to 100 nm in thickness, the presence of larger austenite grains in the microstructure (of the order of micrometres, Fig. 4c) makes the process longer. Besides, transitional carbides and cementite in M1 are known to act as reservoirs of carbon, which may be released again to the system with increasing partitioning times [3]. At 400 °C, this results in the increase of RA fraction and its carbon content with increasing partitioning times.

Partitioning at 500 °C: A small dilatation is observed within the first 2 s of partitioning, which is followed by a continuous contraction. A total shrink of 0.03% is detected after t_P = 300 s. This behaviour results

Table 3
Theoretical calculations of the relative change in length ($\Delta L/L_i$) [46] that can be expected from the different reactions occurring during partitioning at 500 °C. x_C refers to the concentration of carbon and i and f to the initial and final phases, respectively.

	x_C^i wt.%	x_C^{f1} wt.%	x_C^{f2} wt.%	$\frac{\Delta L}{L_i}$ (500 °C) %
1)$\alpha' \rightarrow \alpha + \theta$	0.3	0	6.67	-0.169
2)$\gamma \rightarrow \alpha + \theta$	0.8	0	6.67	0.378
3)$\gamma^+ \rightarrow \gamma + \theta$	1.76	0.6	6.67	-0.834

from simultaneous processes taking place as pointed out in the microstructural characterisation (Fig. 5): 1) martensite tempering, 2) austenite decomposition into pearlite and 3) precipitation of carbides in austenite. In order to gain insight into the microstructural development, theoretical calculations of the relative change in length produced by the different reactions were carried out as explained in Ref. [46]. The results are shown in Table 3. The effect of martensite tempering and cementite precipitation within carbon supersaturated austenite ($\gamma^+ \rightarrow \gamma^- + \theta$) counteract the expansion due to the formation of pearlite, being the precipitation in austenite the main responsible process for the observed contraction. DICTRA simulations show that the carbon enrichment in the austenite next to the γ/α′interfaces or in thin-films can reach values above 1.50 wt % in less than 1 s (Fig. 9b). Calculations at 500 °C with ThermoCalc software (TCFE 9) show that the carbon concentration of austenite in equilibrium with cementite and ferrite is 0.22 and 2.75 wt %, respectively. Additionally, ThermoCalc predicts that the carbon content at which the molar Gibb's free energy for austenite and ferrite are equal at 500 °C is 0.48 wt %. This means that after 1 s of partitioning at 500 °C, the austenite is sufficiently supersaturated in carbon with respect to cementite so that cementite can form. This causes a carbon depletion in the surrounding austenite and thus a contraction in the change in length. Only if the carbon content in the austenite is depleted below 0.48 wt %, the formation of ferrite will be thermodynamically possible. Since no expansion is observed in the present case, it is reasonable to assume that ferrite does not form associated to cementite precipitation within the supersaturated austenite. The fraction of supersaturated austenite is estimated in 0.21 as $f_{\gamma^+} = f_\gamma(t_p = 0) - f_{M2} - f_{RA}$. Considering this fraction of supersaturated austenite and assuming that after precipitation the remaining austenite has the carbon content detected by XRD (0.60 wt %), the precipitation of a $f_\theta \sim 0.20$ is required to match the experimental contraction. In the same manner, the decomposition of austenite into pearlite is possible as the carbon-enriched austenite is simultaneously supersaturated in carbon with respect to both ferrite and cementite [47]. Simulations predict that blocks of austenite of 0.3–0.5 μm in thickness can reach homogeneous carbon concentrations close to the eutectoid composition (0.80 wt % C) within 50 s of partitioning when surrounded by sufficiently large volumes of martensite (block widths of around 1 μm). Thus, these regions would be likely to form pearlite as observed in Fig. 5c.

4.2. Effect of the manganese macrosegregation

4.2.1. Effect on microstructure evolution during the Q&P route

The macrosegregation of Mn plays an important role in the development of the Q&P microstructure. On the one hand, Mn stabilises the austenite phase, reducing the martensite start temperature of the steel. On the other hand, the chemical potential of carbon depends on the local concentration of Mn. During the austenitisation stage at 900 °C, variations in the Mn content due to the macrosegregation in the steel induce a net flux of carbon in order to equalize its chemical potential across austenite regions with different Mn concentrations. This creates an inhomogeneous distribution of carbon.

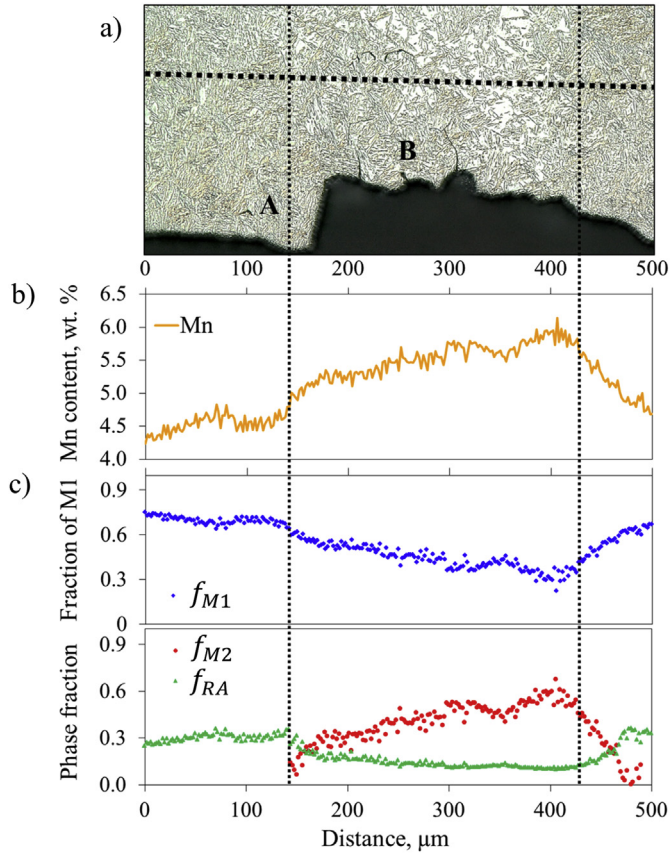

Fig. 10. (a) LOM micrograph perpendicular to the fracture plane in direction of crack propagation of the QP400 condition; (b) EPMA Mn profile along the line in (a); (c) Local Q&P phase fractions along the line in (a).

In order to investigate the effect of manganese segregation on the microstructure evolution, microscopy examination and compositional analysis by electron probe microanalysis (EPMA) were performed on the plane perpendicular to the fracture surface and along the crack propagation direction. The results of QP400 specimen are shown in Fig. 10a. Compositional analysis by EPMA in Fig. 10b shows variations of almost a 2 wt % in Mn, being the presence of RA/M2 islands more evident in the regions where the Mn content is the highest.

To quantify the influence of Mn macrosegregation on the Q&P microstructural development during the thermal cycle, the local phase fractions in the final Q&P microstructure were calculated according to the experimental Mn profiles measured by EPMA. First, DICTRA software (TCFE9 and MOBFE3 data bases) was employed to estimate the concentration of carbon in austenite in dependency with the Mn concentration after austenitisation at 900 °C for 180 s. Since the chemical potential of carbon decreases with increasing the Mn content, Mn-rich regions are slightly enriched in carbon during the austenitisation. Instead, the carbon content in Mn-poor regions decreases. Using ThermoCalc®, variations from 0.32 wt % to 0.30 wt % in carbon are found when moving from a Mn-rich region exhibiting a 6 wt % to a Mn-poor region presenting a 4.30 wt % Mn. Based on these concentration profiles, the martensite start temperature (M_S) was calculated following Andrew's equation [48]:

$$M_S = 539 - 423C - 30.4Mn - 12.1Cr - 17.7Ni - 7.5Mo + 10Co - 7.5\,Si \quad (2)$$

The fraction of primary martensite (f_{M1}) that forms at the quench temperature used in this investigation ($T_Q = 170$ °C) is estimated based on the undercooling below the local M_S according to the Koistinen-Marburger model [49]:

$$f_{M1} = 1 - \exp[-\alpha_m \cdot (T_{KM} - T_Q)] \quad (3)$$

where T_{KM} is the theoretical martensite start temperature, 15–20 °C lower than the M_S for the investigated prior austenite grain size [50, 51], and α_m is the rate parameter, which is calculated based on the local composition using the empirically equation proposed by Van Bohemen et al. [52]:

$$\alpha_m = 0.0224 - 0.0107x_C - 0.0007x_{Mn} - 0.00005x_{Ni} - 0.00012x_{Cr} - 0.0001x_{Mo} \quad (4)$$

For the specimen partitioned at 400 °C, the fractions of RA and M2 were predicted based on the local carbon content and under the assumption of full carbon partitioning, fixed martensite/austenite interface and suppression of competitive reactions as originally proposed by Speer [41]. Fig. 10c shows that the fraction of M1 at the quench temperature decreases significantly in Mn-rich regions. Lower fractions of M1 imply lower fractions of carbon available for the stabilisation of austenite. Therefore, less austenite is retained within the Mn-rich than within Mn-poor regions. Consequently, the fraction of M2 within Mn-rich rises pronouncedly, even exceeding the fraction of M1 in some locations.

For the specimen partitioned at 500 °C, the microstructure evolution cannot be predicted assuming full carbon partitioning since other processes occur during partitioning and consume part of the carbon. The rapid carbon enrichment of austenite and the higher partitioning temperature promote pearlite formation at prior austenite grain boundaries and cementite precipitation within austenite films. However, the Mn macrosegregation is not altered during the partitioning at 500 °C and thus its effect on the microstructural development away from PAGBs can be qualitatively explained in the same manner as at 400 °C. This can be appreciated in the optical micrograph of Fig. 11, where pearlite colonies decorate the PAGBs and a Mn-rich band is disclosed by the presence of large RA/M2 islands.

4.2.2. Effect on the micro-hardness

The fresh martensite phase of Q&P microstructures is a very fine martensite with relatively high carbon content, since it forms from small grains of carbon enriched austenite. The carbon content present in M2 was calculated as 0.55 and 0.50 wt % for the microstructures partitioned at 400 °C and 500 °C, respectively, based on the M_{S2} and applying equation (1). Therefore, M2 is a hard phase compared to the surrounding retained austenite and/or carbon-depleted primary martensite phases. During loading, this difference of strength leads to an inhomogeneous distribution of stresses that decrease the mechanically stability of the austenite and triggers the formation of voids in between M1 and M2 [53,54].

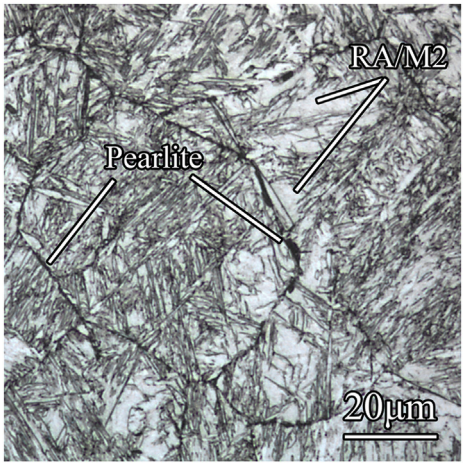

Fig. 11. LOM micrograph of specimen QP500.

Fig. 12 shows LOM micrographs in combination with micro-hardness Vickers maps performed with a load of 0.01 Kg of QP400 and QP500 specimens. A remarkable difference in hardness (more than 200 $HV_{0.01Kg}$) is measured between regions with large fraction of RA/M2 islands and regions in which the predominant phases are tempered M1 and film-type RA. Values as high as 725 $HV_{0.01Kg}$ were locally measured in regions with higher fractions of RA/M2 islands. As expected, this maxima are higher than the average hardness measured in an as-quench specimen (635 ± 5 HV_{1Kg}), i.e. microstructure consisting of fully fresh martensite with the nominal carbon content. The low $HV_{0.01Kg}$ measured in M1 regions is attributed to the effect of tempering, which is evidenced by the presence of carbides in M1 blocks. These large hardness gradients are observed even within one prior austenite grain, as evidenced for the QP500 specimen in Fig. 12b. Despite the prior austenite grains are not revealed in the QP400 microstructure, large hardness gradients are also expected within the prior austenite grains. Therefore, it is concluded that positive Mn segregation increases the local hardness of the Q&P microstructure through the formation of large volume fractions of fresh martensite and, thereby, an influence on the fracture mechanism is expected.

4.3. Fracture mechanisms

The poor elongation exhibited by the medium manganese Q&P steels in this study differs from that of conventional Q&P steels, in which elongations in the order of 20% or higher are obtained [55]. Cho et al. [13] observed a brittle behaviour in a 0.3C-1.6Si−4Mn−1Cr steel subjected to certain Q&P conditions similar to those of the present work; e.g. with T_Q = 170 °C, T_P = 450 °C and t_P = 300 s, a UTS of 1400 MPa and TE of 4% was obtained. They attributed the brittle behaviour to the presence of M2 in the microstructure. However, QP500 specimen, which comprises half of the RA fraction and almost twice the M2 fraction of QP400 specimen, showed improved elongation and toughness. In QP400, the stabilisation of the austenite is more effective than in QP500 and a higher RA fraction, highly enriched in carbon, is obtained. Moreover, in QP400, a RA fraction of 0.10 transforms during deformation (Table 2); however, the low plastic strain observed during tensile testing indicates that this transformation does not contribute effectively to work-hardening. Instead, it might transform during the elastic strain due to low stability of austenite regions with low local carbon concentrations. Moreover, low cohesion strength of prior austenite grain boundaries compared to the strength of the matrix led to intergranular fracture at low strains. This premature failure left an untransformed fraction of RA of 0.19 that does not contribute to work-hardening.

The different fracture mechanisms are also remarkable and are explained based on the different microstructural phenomena taking place during partitioning at 400 °C and 500 °C. The phenomenological analysis of events occurring during partitioning at different temperatures evidences differences in carbon redistribution that strongly influence the microstructure and the mechanical performance:

4.3.1. QP400 fracture mechanism

A magnified view of regions A (rich Mn region) and B (poor Mn region) in Fig. 10a is shown in SEM micrographs of Fig. 13a and Fig. 13b, respectively. The overall crack path is somewhat straight and dominantly intergranular. Crack propagates following prior austenite grains, which is also patent in the progress of secondary cracks (perpendicular to the fracture plane) especially in Mn rich regions. Thus, it is revealed that Mn-rich regions are preferred regions for intergranular fracture. Transgranular fracture was sporadically observed in Mn poor regions, as it is exemplified in Fig. 13b. A plastic deformation is evidenced in M1 laths and RA films adjacent to the crack propagation line. The fracture surface showed micro-dimples at these locations also emphasising the ductile character [54].

Intergranular fracture observed in this steel can be only explained

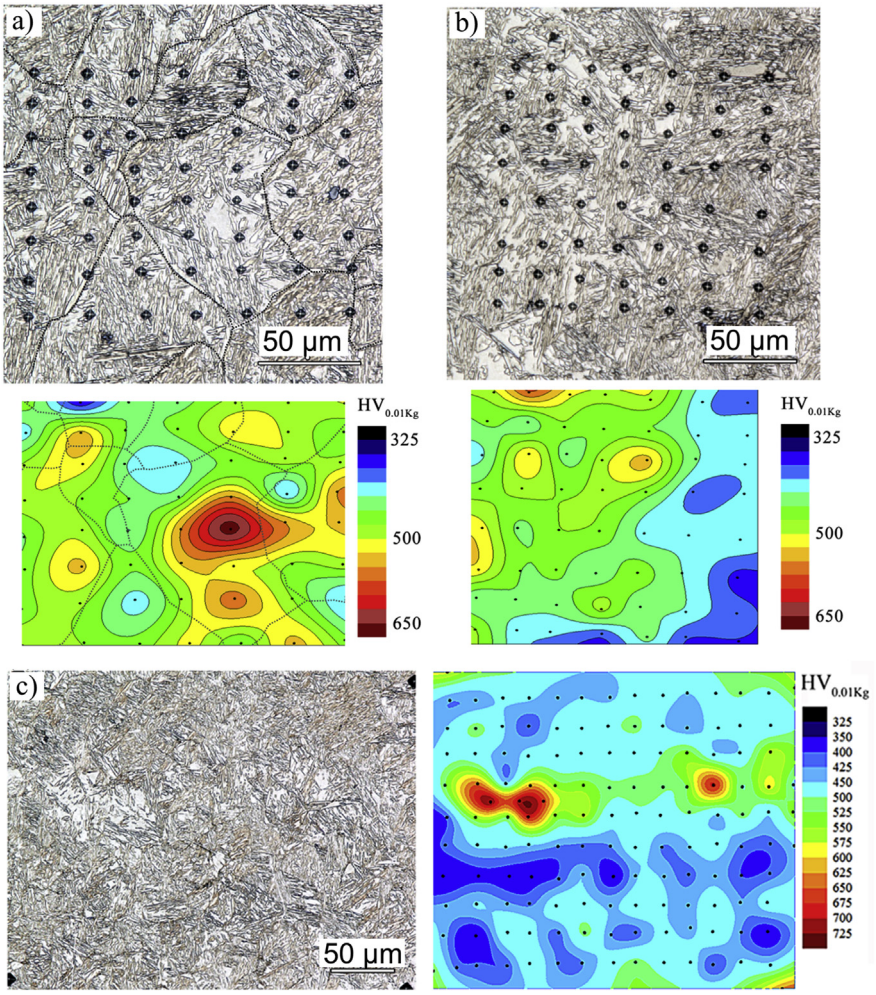

Fig. 12. LOM micrographs showing the region where a the mesh of micro hardness indentations is applied and the corresponding hardness contour maps. (a) QP400 specimen, (b) QP500 specimen high magnification (PAGB are emphasised with a continuous dark line) (c) QP500 low magnification. The following picture is shown in color in the online document.

by a combination of several factors. Elongated precipitates, presumably cementite, were observed at PAGB when this grain boundary is shared by adjacent M1 blocks (Fig. 4). These precipitates have been discussed in relation to intergranular fracture in quenched and tempered martensitic steels [15,37,38,56] as they provide the sites for intergranular grain crack nuclei. Fig. 13b shows a secondary crack connecting with an elongated precipitate at PAGB. Stiff carbide particle is not plastically deformable and will either crack or the martensite/carbide interface will part. The latter separation is more plausible if the interfacial energy has been reduced by segregation of alloying or impurity atoms on it [57]. Intergranular fracture assisted by Mn segregation to austenite grain boundaries has been extensively reported in tempered martensitic steels with additions of silicon and manganese in the range of that of present steels [14,16,17,20,21]. Enrichment of Mn at grain boundaries worsens the grain boundary cohesion, either due to vacancy-Mn pair formation [20], or by grain boundary relaxation [19]. This phenomena can occur even at very low levels of sulphur and phosphorous [14], which in the present material are below 0.003 wt%.

The observed manganese macrosegregation observed plays a double role assisting the intergranular fracture: 1) enhancing the manganese segregation to prior austenite grain boundaries [18,20] and 2) favouring the formation of hard regions as consequence of high fractions

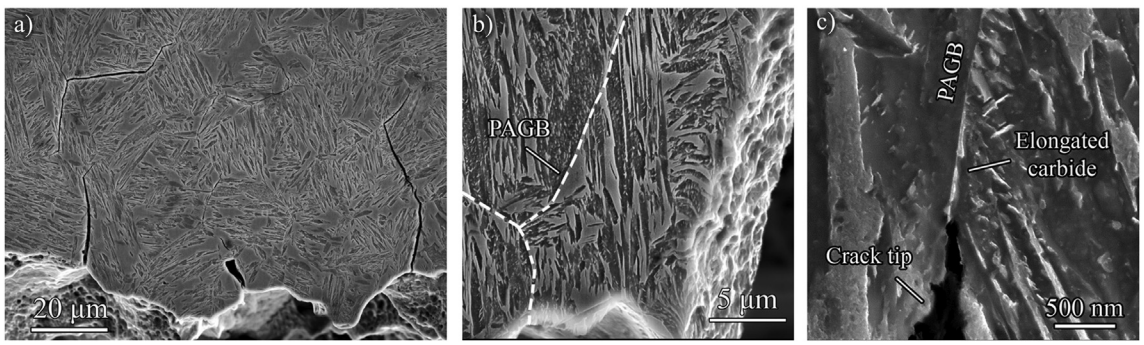

Fig. 13. SEM micrographs of the longitudinal section of the QP400 tensile specimen at break at different locations close to the main crack propagation path.

of M2, as previously discussed. A strong matrix effectively concentrates deformation on the boundaries, which become the weak links. These factors would explain why secondary cracks were mainly observed in Mn-rich regions.

As consequence of previously mentioned factors, cracks can nucleate at low strains and extensively influence other secondary events. A large stress triaxiality may be developed near the crack tip region and thus promote the transformation of RA to martensite. In the present case, micrometre size rings of RA were observed surrounding M2 at large RA/M2 islands characteristic of Mn-rich regions. Due to large size and low carbon content, this austenite has low stability. In turn it may transform into M2 at small deformation assisted by the increasing stress triaxiality. This is evidenced by the high fraction of RA that transforms before premature fracture in QP400 specimen. Xiong et al. [55] recently proposed a similar mechanism occurring in notched Q&P steel specimens which results in the formation of a brittle necklace around a PAGB. Additionally, because of high maximum principle stress, cracks initiate and propagate along this brittle necklace, enhancing the brittle fracture.

4.3.2. QP500 fracture mechanism

The cracks progress mainly transgranularly in QP500 specimens as can be seen in Fig. 14. Secondary cracks are seldom observed and they progress along PAGB or traversing prior austenite grains, as shown respectively in Fig. 14c and d. Instead, several voids are formed at different locations near to the main crack path as exemplified in Fig. 14b. These voids nucleate mainly in locations where M1 and M2/RA are in contact. At these locations, high stresses develop locally during deformation causing the transformation of the low-carbon blocky RA features [54]. Due to martensite formation M2/RA islands strengthen further and thus strain will be preferentially transferred to soft M1 regions.

This change in fracture mechanism is caused by the microstructure changes during partitioning at 500 °C, i.e. mainly by the redistribution of carbon and carbides. The disclosure of prior austenite grain boundaries in QP500 decorated with spherical precipitates, evidences a more severe tempering of the microstructure. Thin precipitates, presumably cementite films, undergo a coarsening process and essentially lose their crystallographic morphology and become more spherical [38]. This process may mitigate the pernicious effect of continuous film-type of carbide at PAGBs and thus explain the appearance of ductile dimples. In QP500 specimen, due to the formation of a high fraction of carbides that are more homogeneously dispersed in the microstructure, the cracks have more paths to initiate and propagate than along the solely prior austenite grain boundaries. The stress necessary for the crack propagation spreads at numerous locations and the cracks progress at higher applied stress, which results in an improved ductility and a more progressive transformation of the RA. The interlath fracture mechanism observed in QP500 can be explained by several microstructural effects that provide additional paths for crack initiation and propagation: 1) Coarse carbides decorating martensite block boundaries, as well as longitudinal arrangements of parallel carbides precipitated from carbon supersaturated thin-films of austenite [58,59], 2) the combination of soft pearlite and adjacent fresh martensite, which results in high local stress levels [6,60]. Additionally, the stress partitioning between RA and M2 at M2/RA islands contributes to a progressive and almost complete transformation of the austenite, as found in other Q&P microstructures [61]. This explains the extended uniform elongation observed in this specimen.

5. Conclusions

The fracture mechanisms that take place in medium-Mn Q&P microstructures created at low (400 °C) and high (500 °C) partitioning temperatures are investigated based on the microstructural development during the Q&P cycle and the influence of Mn macrosegregation present in the initial microstructure.

- The initial microstructure of the steel under investigation exhibits a manganese macrosegregation pattern that consists of Mn-rich intersecting bands, which is typical of forged steels. The macrosegregation is not eliminated during the Q&P cycle. Mn-rich regions exhibit a lower martensite start temperature and thus form lower fractions of primary martensite at the quenching temperature than Mn-poor regions. Therefore, the total fraction of carbon available for partitioning in Mn-rich regions is not sufficient to completely stabilise the austenite during the partitioning step and high fractions of fresh martensite form during the final cooling. Due to a high carbon content in solid solution and a high dislocations density, the fresh martensite and thus the Mn-rich regions exhibit a relatively high

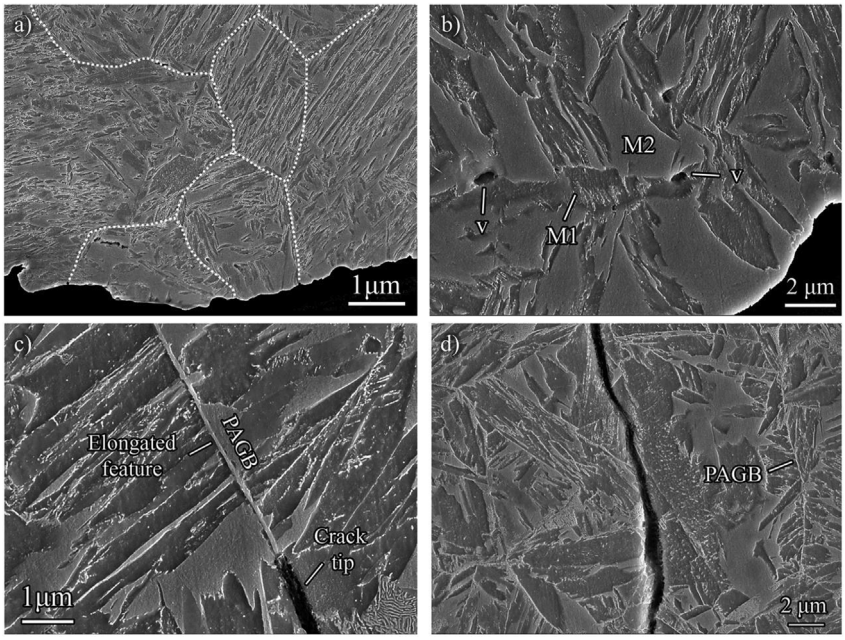

Fig. 14. SEM micrographs of the longitudinal section of the QP500 tensile specimen at break at different locations close to the main crack propagation path.

hardness. In contrast, Mn-poor regions are softer since the tempered primary martensite is the main constituent. Due to this large differences in the local hardness, high local stains gradients develop during testing, which act as voids initiators and reduce the ductility of the Q&P microstructure.

- In microstructures partitioned at 400 °C, an early intergranular failure mechanism is found to disqualify the good mechanical performance of Q&P steels. The cracks progress primarily following the prior austenite grain boundaries (PAGBs), especially around Mn-rich regions. This is associated to the presence of continuous films of carbide at PAGBs, especially when the grain boundary is shared between grains of primary martensite. These films of carbide weaken the PAGBs and facilitate the initiation and progress of the cracks.
- In microstructures partitioned at 500 °C, the fast carbon diffusion kinetics causes a more severe degree of tempering in primary martensite and a rapid carbon enrichment of austenite. The carbon supersaturation of austenite, especially in thin-films and next to the austenite/martensite interface of blocks, triggers the precipitation of parallel particles of cementite and the formation of pearlite. These processes eventually result in a decrease of the retained austenite fraction in the final Q&P microstructure. Yet, microstructures partitioned at 500 °C exhibit improved mechanical and fracture properties than microstructures partitioned at 400 °C. This is associated to the non-connected and dispersed distribution of spherical carbides observed at PAGBs and also at martensite laths/blocks boundaries. This activates the martensite laths/blocks boundaries as additional paths to PAGBs for the nucleation and propagation of cracks. Additionally, the presence of pearlite at PAGBs provides stress partitioning between pearlite/fresh martensite. Eventually, these mechanisms result into a mixed ductile/fragile interlath fracture.

Data availability

The raw and processed data required to reproduce these findings are available to download from http://doi.org/10.4121/uuid:67e93016-8a24-4381-880c-073975797eac.

Acknowledgments

The authors want to acknowledge K. Kwakernaak and R.M. Huizenga for their help and support during the performing of the experimental work and M. Jansen for helping in the analysis of the results. The research leading to these results has received funding from the European Research Council under the European Union's Seventh Framework Programme (FP/2007-2013)/ERC Grant Agreement n. [306292] and the Research Fund for Coal and Steel for funding this research under the Contract RFCS-02-2015 (Project No. 709755).

References

[1] D.K. Matlock, J.G. Speer, Third generation of AHSS: microstructure design concepts, in: A. Haldar, S. Suwas, D. Bhattacharjee (Eds.), Microstructure and Texture in Steels, Springer London, 2009, pp. 185–205.
[2] Y. Toji, G. Miyamoto, D. Raabe, Carbon partitioning during quenching and partitioning heat treatment accompanied by carbide precipitation, Acta Mater. 86 (2015) 137–147.
[3] F. HajyAkbary, J. Sietsma, G. Miyamoto, T. Furuhara, M.J. Santofimia, Interaction of carbon partitioning, carbide precipitation and bainite formation during the Q&P process in a low C steel, Acta Mater. 104 (2016) 72–83.
[4] A.S. Nishikawa, M.J. Santofimia, J. Sietsma, H. Goldenstein, Influence of bainite reaction on the kinetics of carbon redistribution during the Quenching and Partitioning process, Acta Mater. 142 (2018) 142–151.
[5] M.J. Santofimia, J.G. Speer, A.J. Clarke, L. Zhao, J. Sietsma, Influence of interface mobility on the evolution of austenite–martensite grain assemblies during annealing, Acta Mater. 57 (2009) 4548–4557.
[6] D. De Knijf, R. Petrov, C. Föjer, L.A.I. Kestens, Effect of fresh martensite on the stability of retained austenite in quenching and partitioning steel, Mater. Sci. Eng. 615 (2014) 107–115.
[7] Y. Tomota, H. Tokuda, Y. Adachi, M. Wakita, N. Minakawa, A. Moriai, Y. Morii, Tensile behavior of TRIP-aided multi-phase steels studied by in situ neutron diffraction, Acta Mater. 52 (2004) 5737–5745.
[8] D. De Knijf, E.P. Da Silva, C. Föjer, R. Petrov, Study of heat treatment parameters and kinetics of quenching and partitioning cycles, Mater. Sci. Technol. 31 (2015) 817–828.
[9] I. De Diego-Calderón, D. De Knijf, J.M. Molina-Aldareguia, I. Sabirov, C. Föjer, R. Petrov, Effect of Q&P parameters on microstructure development and mechanical behaviour of Q&P steels, Rev. Metal. (Madr.) 51 (2015).
[10] Z.H. Cai, H. Ding, X. Xue, J. Jiang, Q.B. Xin, R.D.K. Misra, Significance of control of austenite stability and three-stage work-hardening behavior of an ultrahigh strength–high ductility combination transformation-induced plasticity steel, Scripta Mater. 68 (2013) 865–868.
[11] B.L. Ennis, E. Jimenez-Melero, E.H. Atzema, M. Krugla, M.A. Azeem, D. Rowley, D. Daisenberger, D.N. Hanlon, P.D. Lee, Metastable austenite driven work-hardening behaviour in a TRIP-assisted dual phase steel, Int. J. Plast. (2017) 88.
[12] E.J. Seo, L. Cho, B.C. De Cooman, Application of quenching and partitioning processing to medium Mn steel, Metall. Mater. Trans.: Phys. Metall. Mater. Sci. 46 (2015) 27–31.
[13] L. Cho, E.J. Seo, B.C. De Cooman, Near-Ac3 austenitized ultra-fine-grained quenching and partitioning (Q&P) steel, Scripta Mater. 123 (2016) 69–72.
[14] J.D. Bolton, E.R. Petty, G.B. Allen, The mechanical properties of α-phase low-carbon Fe-Mn alloys, Metall. Trans. 2 (1971) 2915–2923.
[15] R.M. Horn, R.O. Ritchie, Mechanisms of tempered martensite embrittlement in low alloy steels, Metall. Trans. 9 (1978) 1039–1053.
[16] H.J. Grabke, K. Hennesen, R. Möller, W. Wei, Effects of manganese on the grain boundary segregation, bulk and grain boundary diffusivity of P in ferrite, Scripta Metall. 21 (1987) 1329–1334.
[17] R.L. Bodnar, T. Ohhashi, R.I. Jaffee, Effects of Mn, Si, and purity on the design of 3.5NiCrMoV, 1CrMoV, and 2.25Cr-1Mo bainitic alloy steels, Metall. Trans. 20 (1989) 1445–1460.
[18] M. Nasim, B.C. Edwards, E.A. Wilson, A study of grain boundary embrittlement in an Fe–8%Mn alloy, Mater. Sci. Eng. 281 (2000) 56–67.
[19] R. Yang, D.L. Zhao, Y.M. Wang, S.Q. Wang, H.Q. Ye, C.Y. Wang, Effects of Cr, Mn on the cohesion of the γ-iron grain boundary, Acta Mater. 49 (2001) 1079–1085.
[20] M. Kuzmina, D. Ponge, D. Raabe, Grain boundary segregation engineering and austenite reversion turn embrittlement into toughness: example of a 9wt.% medium Mn steel, Acta Mater. 86 (2015) 182–192.
[21] F. Archie, X. Li, S. Zaefferer, Micro-damage initiation in ferrite-martensite DP microstructures: a statistical characterization of crystallographic and chemical parameters, Mater. Sci. Eng. 701 (2017) 302–313.
[22] A. Kwiatkowski da Silva, G. Inden, A. Kumar, D. Ponge, B. Gault, D. Raabe, Competition between formation of carbides and reversed austenite during tempering of a medium-manganese steel studied by thermodynamic-kinetic simulations and atom probe tomography, Acta Mater. 147 (2018) 165–175.
[23] J. Mola, B.C. De Cooman, Quenching and partitioning (Q&P) processing of martensitic stainless steels, Metall. Mater. Trans. 44 (2013) 946–967.
[24] G. Krauss, Solidification, segregation, and banding in carbon and alloy steels, Metall. Mater. Trans. B 34 (2003) 781–792.
[25] R.A. Grange, Effect of microstructural banding in steel, Metall. Trans. 2 (1971) 417–426.
[26] F. HajyAkbary, J. Sietsma, R.H. Petrov, G. Miyamoto, T. Furuhara, M.J. Santofimia, A quantitative investigation of the effect of Mn segregation on microstructural properties of quenching and partitioning steels, Scripta Mater. 137 (2017) 27–30.
[27] L. Zhao, N.H. Van Dijk, E. Brück, J. Sietsma, S. Van Der Zwaag, Magnetic and X-ray diffraction measurements for the determination of retained austenite in TRIP steels, Mater. Sci. Eng. 313 (2001) 145–152.
[28] A. Bojack, L. Zhao, P.F. Morris, J. Sietsma, In-situ determination of austenite and martensite formation in 13Cr6Ni2Mo supermartensitic stainless steel, Mater. Char. 71 (2012) 77–86.
[29] T.T.W. Koopmans, Thermal stability of retained austenite in Quenching & Partitioning steels, MSc Thesis, Materials Science and Engineering Department, TU Delft, Delft, 2015.
[30] B.D. Cullity, C.D. Graham, Introduction to Magnetic Materials, second ed., (2009) (Hoboken, N.J).
[31] N.H. Van Dijk, A.M. Butt, L. Zhao, J. Sietsma, S.E. Offerman, J.P. Wright, S. Van Der Zwaag, Thermal stability of retained austenite in TRIP steels studied by synchrotron X-ray diffraction during cooling, Acta Mater. 53 (2005) 5439–5447.
[32] J.B. Nelson, D.P. Riley, An experimental investigation of extrapolation methods in the derivation of accurate unit-cell dimensions of crystals, Proc. Phys. Soc. 56 (1945) 160–176.
[33] J.T. Armstrong, Quantitative elemental analysis of individual microparticles with electron beam instruments, in: K.F.J. Heinrich, D.E. Newbury (Eds.), Electron Probe Quantitation, Springer US, Boston, MA, 1991, pp. 261–315.
[34] M.J. Santofimia, L. Zhao, J. Sietsma, Volume change associated to carbon partitioning from martensite to austenite, Materials Science Forum, 2012, pp. 2290–2295.
[35] M.J. Santofimia, L. Zhao, R. Petrov, C. Kwakernaak, W.G. Sloof, J. Sietsma, Microstructural development during the quenching and partitioning process in a newly designed low-carbon steel, Acta Mater. 59 (2011) 6059–6068.
[36] M.J. Santofimia, L. Zhao, R. Petrov, J. Sietsma, Characterization of the microstructure obtained by the quenching and partitioning process in a low-carbon steel, Mater. Char. 59 (2008) 1758–1764.
[37] S. Yusa, T. Hara, K. Tsuzaki, T. Takahashi, Refinement of grain boundary cementite in medium-carbon tempered martensite by thermomechanical processing, Mater. Sci. Eng. 273–275 (1999) 462–465.

[38] H.K.D.H. Bhadeshia, S.R. Honeycombe, 9 - the tempering of martensite, Steels, third ed., Butterworth-Heinemann, Oxford, 2006, pp. 183–208.
[39] M. Janssen, J. Zuidema, R.J.H. Wanhill, Fracture Mechanics, second ed., VSSD, Delft, The Netherlands, 2006.
[40] D. Said Schicchi, F. Hoffmann, F. Frerichs, A mesoscopic approach of the quench cracking phenomenon influenced by chemical inhomogeneities, Eng. Fail. Anal. 78 (2017) 67–86.
[41] J.G. Speer, F.C. Rizzo Assunção, D.K. Matlock, D.V. Edmonds, The "quenching and partitioning" process: background and recent progress, Mater. Res. 8 (2005) 417–423.
[42] A. Borgenstam, L. Höglund, J. Ågren, A. Engström, DICTRA, a tool for simulation of diffusional transformations in alloys, J. Phase Equilibria 21 (2000) 269.
[43] C.A. Apple, R.N. Caron, G. Krauss, Packet microstructure in Fe-0.2 pct C martensite, Metall. Trans. 5 (1974) 593–599.
[44] T. Swarr, G. Krauss, The effect of structure on the deformation of as-quenched and tempered martensite in an Fe-0.2 pct C alloy, Metall. Trans. 7 (1976) 41–48.
[45] A.J. Clarke, J.G. Speer, D.K. Matlock, F.C. Rizzo, D.V. Edmonds, M.J. Santofimia, Influence of carbon partitioning kinetics on final austenite fraction during quenching and partitioning, Scripta Mater. 61 (2009) 149–152.
[46] T. Nguyen-Minh, Quenching and Partitioning of low alloyed steels, Materials Science and Engineering, TU Delft, Delft, 2008.
[47] D.A. Porter, K.E. Easterling, Phase Transformations in Metals and Alloys, second ed., Chapman and Hall, London, 1992.
[48] K.W. Andrews, Empirical formulae for the calculation of some transformation temperatures, J. Iron Steel Inst. 203 (1965) 721–727.
[49] D.P. Koistinen, R.E. Marburger, A general equation prescribing the extent of the austenite-martensite transformation in pure iron-carbon alloys and plain carbon steels, Acta Metall. 7 (1959) 59–60.
[50] J. Sietsma, Kinetics of martensite formation in plain carbon steels: critical assessment of possible influence of austenite grain boundaries and autocatalysis AU - van Bohemen, S. M. C, Mater. Sci. Technol. 30 (2014) 1024–1033.
[51] C. Celada-Casero, J. Sietsma, M.J. Santofimia, Mater. Des. (2019) 107625.
[52] S.M.C. van Bohemen, J. Sietsma, Effect of composition on kinetics of athermal martensite formation in plain carbon steels, Mater. Sci. Tech. Ser. 25 (2009) 1009–1012.
[53] D. De Knijf, R. Petrov, C. Föjer, L.A.I. Kestens, Effect of fresh martensite on the stability of retained austenite in quenching and partitioning steel, Mater. Sci. Eng. 615 (2014) 107–115.
[54] M.M. Wang, J.C. Hell, C.C. Tasan, Martensite size effects on damage in quenching and partitioning steels, Scripta Mater. 138 (2017) 1–5.
[55] Z. Xiong, P.J. Jacques, A. Perlade, T. Pardoen, Ductile and intergranular brittle fracture in a two-step quenching and partitioning steel, Scripta Mater. 157 (2018) 6–9.
[56] N. Bandyopadhyay, C.J. McMahon, The micro-mechanisms of tempered martensite embrittlement in 4340-type steels, Metall. Trans. A. 14 (1983) 1313–1325.
[57] H. Bhadeshia, R. Honeycombe, Chapter 9 - tempering of martensite, in: H. Bhadeshia, R. Honeycombe (Eds.), Steels: Microstructure and Properties, fourth ed., Butterworth-Heinemann, 2017, pp. 237–270.
[58] G. Krauss, Deformation and fracture in martensitic carbon steels tempered at low temperatures, Metall. Mater. Trans. B Process Metall. Mater. Process. Sci. 32 (2001) 205–221.
[59] H.K.D.H. Bhadeshia, D.V. Edmonds, Tempered martensite embrittlement: role of retained austenite and cementite, Met. Sci. 13 (1979) 325–334.
[60] A. Varshney, D. Verma, S. Sangal, K. Mondal, High strength high carbon low alloy pearlite-ferrite-tempered martensite steels, Trans. Indian Inst. Met. 68 (2015) 117–128.
[61] K.O. Findley, J. Hidalgo, R.M. Huizenga, M.J. Santofimia, Controlling the work hardening of martensite to increase the strength/ductility balance in quenched and partitioned steels, Mater. Des. 117 (2017) 248–256.